Polymorphism of group-IV carbides: Structures, (meta)stability, electronic, and transport properties

Matthew Jankousky ⬤, Emily M. Garrity ⬤, and Vladan Stevanović ⬤[*]
Colorado School of Mines, Golden, Colorado 80401, USA

Herein we investigate the spectra of crystal structures and their metastability for elemental carbon and the entire set of group-IV monocarbides (SiC, GeC, and SnC) using the *ab initio* random structure sampling. All of the known structures of elemental C and SiC are correctly identified as high probability in the random sampling and the predicted metastabilities of polymorphs are consistent with the existing knowledge. Furthermore, we find the same four structure types, tetrahedrally bonded zincblende, wurtzite, and rhombohedral-$R\bar{3}m$, as well as octahedrally coordinated rocksalt at high pressure, as the only relevant polymorphs for all studied carbides. However, the rocksalt structure in GeC is shown to be dynamically unstable, contrary to SiC and SnC. Additionally, all GeC and SnC structures are found to have positive enthalpies of formation and are therefore unstable relative to decomposition. The tetrahedrally bonded polymorphs, especially the SnC ones, are predicted to have very high intrinsic (phonon-limited) electron mobilities comparable with the best known semiconductors. Additionally, wurtzite SnC is lattice matched to InN suggesting epitaxial growth as a possible avenue to realize wurtzite SnC.

I. INTRODUCTION

Structure predictions have accelerated the search for novel materials by providing a relatively rapid strategy to predict new stable compounds and to screen for useful properties [1,2]. These computations have informed the creation of new and promising materials, and continue to provide a foundational understanding of the composition-structure-property relationships [3–5]. However, the space of metastable polymorphs, those structures that are long-lived at conditions at which they do not represent the global minimum of the relevant thermodynamic potential, remains largely uninvestigated. This is mainly because identification of experimentally realizable and long-lived states from among a large number of possible low-energy structures represents a challenge for computational searches [6–8].

The group-IV carbides, including elemental carbon, SiC, GeC, and SnC, represent a compelling chemical space for testing our current understanding of the phenomenon of metastability, computational methods for identifying realistic metastable states, as well as to search for novel functional metastable polymorphs. This is because (a) a number of metastable polymorphs are experimentally observed in all of the group-IV elemental substances [9,10] as well as in SiC [11], and (b) some of the previously realized materials from this group such as diamond (d-C) and various polymorphs of SiC are known to be good semiconductor materials thanks to their high electron mobilities, band gaps in desirable ranges, and their dopability [12,13]. Polymorphism is particularly relevant to this group of binary compounds given that the SiC structure which performs best in power electronic applications

used in commercial devices is a metastable wurtzite (4H) polymorph, and not the ground-state zincblende (3C) structure [14]. Finally, regarding possible applications, the group-IV compounds are earth abundant and nontoxic.

Elemental carbon is well recognized for its rich polymorphism. Experimentally realized 3D crystalline structures include various versions of graphite with space group numbers (s.g. #s) 194 and 166, cubic and hexagonal diamonds (s.g. #s 227 and 194, respectively), and so on. Among the carbides, the well-studied SiC composition has three common tetrahedrally bonded metastable polymorphs: the zincblende ground state with the s.g. #216 often labeled as 3C [11,15–19], wurtzite structure (s.g. #186 or 2H) [11,16,17,19,20], and the rhombohedral structure (s.g. #160 or 15R) [11,19]. All of them exhibit rich polytypism, that is, periodic arrangement of stacking faults along particular directions leading to a range of derivative structures such as 4H, 6H, and 8H wurtzite derivatives, or 21R and 24R rhombohedral derivatives. In addition, the high-pressure rocksalt phase (s.g. #225) is another experimentally realized structure [17–19], but is relatively short lived at ambient conditions. These four structure types (zincblende, wurtzite, rhombohedral, and rocksalt) are shown in Fig. 1. On the other hand, not much is known about the relevant structures and polymorphism of GeC and SnC. Experimentally, GeC is realized in the zincblende structure primarily as a thin film [21–24] or as an alloy with SiC [25,26], while SnC has not been realized to our knowledge. Hence, it is natural to ask: do GeC and SnC share the same polymorphism as SiC?

Herein, we systematically investigate the polymorphism and search for new experimentally realizable and potentially useful metastable structures in these chemistries. To do this we employ the *ab initio* random structure sampling [6,27]. This method generates a large set of random structures (random lattice vectors and atomic positions) for a given chemistry
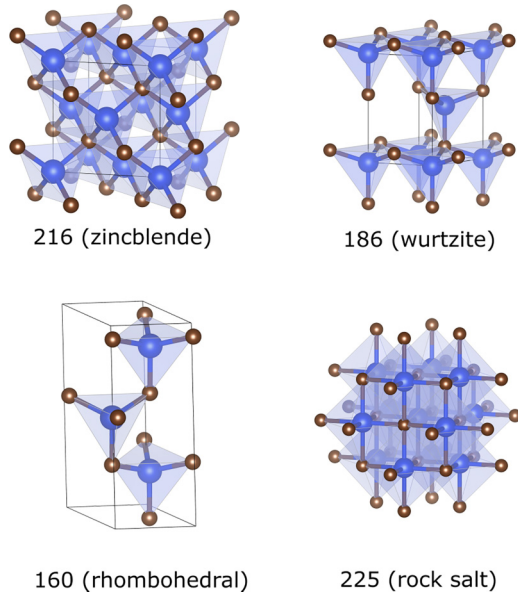
---
*vstevano@mines.edu

FIG. 1. The four known structure types of SiC, zincblende (s.g. #216 or 3C), wurtzite (s.g. #186 or 2H), rhombohedral (s.g. #160 or 9R), and rocksalt (s.g. #225). The numbers in the labels for the H and R structures denote the number of formula units in the conventional unit cell (may be less in the primitive cell).

and stoichiometry, which are then relaxed using density functional theory [28] to the respective closest local minimum on the potential energy surface. The structures are then grouped according to the unique structure types and the experimental realizability is assessed using statistical ensemble probabilities within the isobaric-isothermal ensemble. Previous work has shown that structures with the highest ensemble probabilities are the most likely to be experimentally realized, as demonstrated for MgO, ZnO, SnO_2 [27], elemental Si [29], SnN [30], and in this paper for elemental carbon and SiC. Furthermore, this methodology has accurately reproduced the structural features of glassy systems [31] and explained the experimentally observed stability of the disordered rocksalt phase relative to the ordered ground-state "wurtsalt" structure for $ZnZrN_2$ [32].

Another requirement to classify a phase as metastable is its lifetime. Phases with short lifetimes are limited in their applications as they can rapidly transform to either the ground state or another metastable phase. In this paper, we use a recently developed code and heuristic to generate optimal atom-to-atom maps between phases and to classify those transformations as rapid or sluggish [33,34]. This heuristic states that if the optimal atom-to-atom map demonstrates nonmonotonic changes in atomic coordination, the energy barrier for this transformation is likely to be high and the transformation is likely to be sluggish, while monotonic coordination changes suggest a low energy barrier and rapid transformation. Under the assumption of the collective (concerted) movement of atoms during the phase transformation, the upper bound of the energy barrier can be approximated to first order by calculating the DFT energy of the structures along the optimal atom-to-atom map. This approach has led to accurate classification of structures as long lived

(cristobalite to quartz in SiO_2, diamond to graphite) or short lived (rocksalt to zincblende, rocksalt to wurtzite, CsCl to NaCl) [33].

In short, our approach reproduces the known polymorphism of elemental C and SiC well. We also find that the tetrahedrally coordinated structures (s.g. #216, #186, and #160) are the only relevant high-symmetry crystalline phases for GeC and SnC, too. The octahedrally coordinated rocksalt structure (s.g. #225) is found to be a dynamically stable high-pressure phase for SiC and SnC, while that is not true for GeC. Transformation pathways that are likely to be rapid are found between rocksalt and each of the three tetrahedrally bonded structures, suggesting that rocksalt is not a long-lived metastable phase in any of these chemistries. This corroborates the observed experimental behavior in SiC: if pressure is released from a sample in the rocksalt phase, the sample will relax to one of the tetrahedrally coordinated structures [19]. Transformations between tetrahedrally bonded structures are all predicted to be slow, consistent with the experimental observation that the wurtzite and rhombohedral phases are long lived. Contrary to SiC and GeC, neither zincblende, nor wurtzite, nor rhombohedral are the high-probability structures for SnC. We find the low-symmetry phase-separated solutions to be more probable, consistent with the lack of experimental realization of SnC. However, we find that zincblende SnC has exceptionally high predicted intrinsic electron mobility and wurtzite SnC is well lattice matched to wurtzite InN [35,36], suggesting epitaxial growth of thin films as a possible avenue to realize SnC and utilize its promising electron transport properties.

II. METHODS

A. Random structure sampling

The statistical (probabilistic) description of the experimental realizability of metastable structures, developed previously [29] and used in this paper, requires having a complete set of statistically relevant local minima and their degeneracies. This is achieved through *ab initio* random structure sampling in the following way. A large set of structures with predefined number of atoms, random unit cell vectors, and random positions of the atoms is created and then fully relaxed using *ab initio* methods, most often based on density functional theory (DFT) [28]. If gradient-based relaxation of the cell parameters and atomic positions is employed, the structures are most likely to relax to the local minimum closest to the initial random structure. Then, the structures that occur more frequently than the rest are the statistically relevant ones [27]. Greater frequency implies that those structures have attraction basins on the potential energy surface occupying larger portions of the configuration space. Once the set of these relevant structures and their frequencies of occurrence is converged with respect to the total number of random structures, a reliable statistical description can be formulated as described in Sec. II B.

The method for random structure generation and relaxation is developed and described in greater detail in Refs. [27,29]. In short, we employ a modified version of the *ab initio* random structure sampling, which we call random superlattices, developed to bias the random structure generation toward a
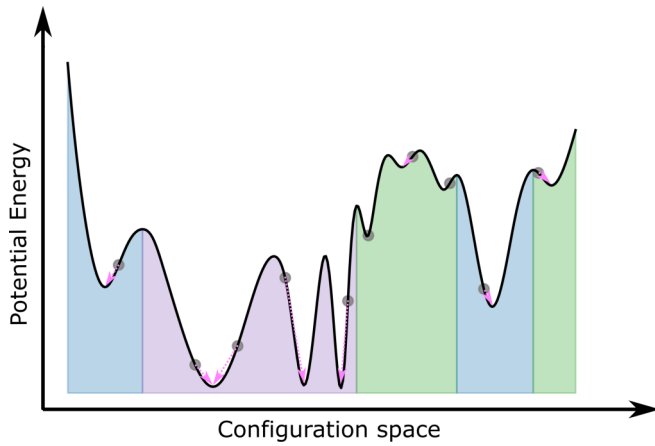
FIG. 2. Random sampling creates configurations (gray circles), which relax to the minimum of their potential energy well (pink arrows). There may be many wells with similar depths but varying widths whose probabilities of realization may be different even though their energies are comparable (purple region). There also exist many shallow, narrow wells that are often unlikely, disordered structures (green regions), and wells with intermediate probabilities due to their depth and/or width, which may be realizable under different conditions (blue regions).

situation in which unlike atoms are coordinated with each other. This is particularly useful when dealing with partially ionic systems where cation-anion coordination is favored because of charge transfer and Coulomb interactions. We achieve this by distributing cations and anions randomly over two interpenetrating grids of points belonging to a superlattice constructed using a random reciprocal lattice vector. In this way the sampling is narrowed to a more relevant part of the potential energy surface and converged results can be achieved with a reasonable number of structures. For carbon, this procedure is equivalent to a normal random structure generation procedure, while it accelerates the convergence of the random sample for SiC, GeC, and SnC because of their partially ionic character [37].

After the relaxations are completed the structures are grouped into classes of equivalent local minima based on their total energy, space group assignment, volume, and the coordination of atoms (first two shells). The grouping allows evaluation of the degeneracies for each local minimum by counting the number of structures in each group. The sampling is considered converged when the relative frequencies of occurrence of the most frequent local minima stop changing appreciably as a function of the total number of random structures, which is typically achieved after relaxing several thousand random structures. Subsequently, the statistical treatment of the results is performed as described in the next section.

B. Statistical description of polymorph realizability

Converged random structure sampling provides a sample of the relevant portion of the potential energy surface as illustrated in Fig. 2. The partition function within the isobaric-isothermal thermodynamic ensemble formalism can then be evaluated as

$$Z = \sum_i g_i e^{-\frac{E_i + pV_i}{kT}}, \quad (1)$$

where g_i is the degeneracy of the structure indexed i (frequency of occurrence in the random sampling), E_i is its total energy per formula unit relative to the ground state, p is the pressure, and V_i is its volume per formula unit. The corresponding ensemble probability for each structure is then

$$\mathcal{P}_i = \frac{1}{Z} g_i e^{-\frac{E_i + pV_i}{kT}}. \quad (2)$$

The isothermal-isobaric ensemble, in which enthalpy $H = E + pV$ is used to compute ensemble probabilities of each structure, is adopted in our work following the detailed discussion in Ref. [31]. The isothermal-isobaric ensemble is an appropriate choice given that different polymorphs have different volumes. However, when evaluating the ensemble probabilities, we will assume low pressure ($p \approx 0$). While strictly speaking, the ergodic hypothesis of statistical mechanics does not apply in crystalline solids because of the kinetic barriers between different local minima, it has been shown previously that the ensemble probabilities as defined by Eq. (2) provide a reliable ranking of different structures in terms of their experimental realizability [27,29,30]. As we will show later, this is also the case for elemental carbon and SiC. Furthermore, it was also shown that if ergodicity is fully adopted then the structural features of the statistical mixture of different local minima obtained by the random structure sampling correspond well to those of the amorphous/glassy state [31]. The use of ensemble probability in the context of assessing/predicting the chances for experimental realization of (potentially) metastable structures is rooted in their physical interpretation within the framework of statistical mechanics. Namely, ensemble probabilities measure the probability of finding the system in a particular state and in addition to energy also take into account, within our formalism, the configurational entropy, both of which were shown in our previous works to be important.

As discussed previously in Ref. [8] the approach adopted here has clear advantages over the attempts to reduce the phenomenon of metastability only to the energy above the ground state. These attempts have two major weaknesses. First, by defining various energy scales or limits of metastability and neglecting entropy or other contributions to thermodynamic potentials one inevitably undervalues those other contributions, which can be critical. For example, in high-pressure experiments the $p\Delta V$ term can reach multiple electron volts as can be illustrated by the following "back of the envelope" estimate. If one simply multiplies the volume difference between graphite and diamond (≈ 3 Å^3/atom) by a relatively high, but experimentally achievable pressure of 100 GPa, ≈ 0.6 eV/Å^3, one finds that an energy difference larger than 1.5 eV/atom can be overcome by pressure, which is an order of magnitude or more above the proposed energy limits. It is then not a surprise that many known high-pressure phases show up manifestly above the amorphous limits of Ref. [38] prompting the authors to declare them as an exception to the rule. Second, even if we accept the energy limits as approximately accurate, they are just limits and say nothing about

why the majority of the many low-energy local minima that are readily found in structure predictions are never experimentally realized and/or observed. Our approach, rooted in statistical ensemble probabilities naturally includes the energy above the ground state as well as configurational entropy and can accommodate any other contribution to thermodynamic potentials including $p\Delta V$ and others, just by following standard statistical mechanics. The high-pressure phases are also naturally included in our approach as discussed in this paper (rocksalt phase) and elsewhere [8,29]. Additionally, our approach is shown to be capable of resolving which of the many low-energy structures have higher chances for experimental realization.

C. Lifetime assessment

To estimate whether transformations between phases are likely to be slow or fast, optimal atom-to-atom maps were predicted and analyzed. In this context, slow means that a phase is likely to persist far from the conditions at which it is the global minimum of the relevant thermodynamic potential, while fast means that a phase will relax to the global minimum with a relatively short lifetime. The optimal atom-to-atom relationships are generated by the *pmpaths* code [33], which establishes a correspondence (a map) between the atoms from the initial and the final structures by minimizing the distance they need to travel from one structure to the other. The mapping is performed with the full account of the periodic boundary conditions as explained in more detail in Ref. [33], which results in transformation pathways similar to the maximal symmetry transformation pathways by Capillas *et al.* [39]. While herein we are more interested in qualitatively classifying transformation pathways into rapid and sluggish cases, for which the described mapping is shown to work well [33], more realistic results closer to the actual nucleation and growth processes can be achieved by abandoning periodic boundary conditions as explained in Refs. [34,40]. The qualitative classification follows from the change in coordination (more precisely, the number of chemical bonds) along the pathways. If the change in number of chemical bonds along the pathway is monotonic, the transition is expected to be rapid, while if the change in number of chemical bonds along the pathway is nonmonotonic, the transition is expected to be slow (sluggish). This is because the breaking of excess chemical bonds results in a significant energetic penalty for the pathway. For the SiC structures, the energy of the images along the pathways were also calculated using DFT (without any relaxations) and were found to corroborate the qualitative estimate.

D. Transport property calculations

To understand properties of these systems relevant to semiconductor performance, we compute the electron-phonon limited drift and Hall mobilities of the zincblende (s.g. # 216) structures using the EPW (electron-phonon coupling using Wannier functions) code [41–45] of the Quantum Espresso Suite [46–48]. This is done by iteratively solving the Boltzmann transport equation. The scattering rate is computed by integrating over a dense grid of electron-phonon coupling constants that is computed using Wannier interpolation over coarse grids of k and q points. For all structures (3C, 2H, and 9R in SiC, GeC, and SnC, as well as 4H, 6H, and 15R in SiC), a semiempirical model for the electron mobility is used to provide a first-order estimate because of the computational expense of running EPW.

The semiempirical model for mobility is applied as in Ref. [49] and revised in Ref. [50]. This model assumes constant relaxation time and that scattering is dominated by electron-phonon effects rather than ionized impurities. Because the relaxation time associated with phonon scattering in the acoustic and optical deformation potentials can be shown to be proportional to elastic constants, the model correlates mobility to the bulk modulus as well as the band effective mass.

We also evaluate the Baliga figure of merit (BFOM) using both first-principles and semiempirical mobilities. The BFOM is used to predict the performance of these materials in low-frequency power electronic applications. The n-type and p-type BFOM are calculated as

$$BFOM = E_b^3 \mu \varepsilon \tag{3}$$

where E_b is the critical electric field at avalanche breakdown, μ is the carrier mobility (either electrons or holes), and ε is the dielectric constant [51]. The breakdown field is estimated using a machine-learned model from Ref. [52] trained on data produced using the first principles calculations in Ref. [53]. The first-principles calculations rely on the assumption that breakdown occurs when the average energy gain from the electric field exceeds the average energy lost due to phonon collisions. As a result, the machine-learned model finds that breakdown field can be estimated as a function of band gap (related to average energy gain) and maximum optical phonon frequency (related to energy lost due to phonon scattering).

E. Calculation parameters

For each of SiC, GeC, and SnC, 12-atom (six formula units) supercells were used and 2000 random (superlattice) structures are generated. For elemental carbon 5000 12-atom structures were generated. This number of structures was found to be sufficient such that the frequencies of occurrence are converged with respect to the total number of structures. Plots of the frequencies of occurrence against the total number of structures are included in Fig. S1 of the Supplemental Material [54]. The 5000 structures used for elemental carbon are more than enough to provide a proof of concept for the rest of the chemistries explored. All structures considered in this study have 12 atoms in order to balance the computational expense of relaxing thousands of structures with having enough degrees of freedom to get diverse structures and having a unit cell that is compatible with the known polymorphs.

Random structures are fully relaxed, including both cell parameters and atomic positions, using the VASP code [55–58]. Relaxations are performed using the conjugate gradient algorithm to ensure that most structures relax to their nearest local minimum [59]. Given that random structure generation sometimes produces structures that are difficult to relax, we consider the relaxations finished when at least 90% of all of the random structures in the samples are fully relaxed. All

analysis is performed on the set of those structures. Relaxations are considered converged when the difference in energy between ionic steps is less than 1e–6 eV/atom. They were performed with an automatically generated k-point grid with length parameter 20, and a plane wave energy cutoff of 840 eV for elemental C, and 340 eV for SiC, GeC, and SnC. The difference in the cutoffs is due to different pseudopotentials used. Namely, for elemental carbon we found that the hard (C_h) pseudopotential is necessary because of the short C-C bond lengths, while for SiC our initial tests showed no significant difference between the pseudopotentials, which allowed the use of the least computationally expensive ones (i.e., the soft). For all C calculations the opt86b-vdW-DFT routine by Klimeš was used [60,61] to better describe the van der Waals interactions known to be of importance for many structures of elemental carbon. This functional has demonstrated good performance for diverse structures of elemental carbon including diamond [60], and graphite and related structures [62,63]. All calculations for this paper were performed using the generalized gradient approximation (GGA) [64] within the projector augmented wave (PAW) formalism [65] with the Perdew-Burke-Ernzerhoff (PBE) exchange-correlation functional [64]. The calculations and analysis in a high-throughput workflow were managed using the computational materials framework *pylada* [66].

After the relaxations were completed we classified structures into classes of equivalence using the following definition. Two structures are considered equivalent if their space group assignment (using the spglib library [67] with the symmetry precision of 0.2 Å) is the same, their total energies per atom are within 0.01 eV, their volumes do not differ by more than 1.5%, and average coordination in the first and the second shell for all atom types is the same. These conditions are sufficient to accurately distinguish various structure types, but are also not too strict and able to accommodate small numerical differences that are inevitably present. In particular, in the van der Waals bonded structures of elemental carbon, the potential energy surface is relatively flat, so structures with different relative positions of van der Waals planes can be very close in energy. These changes in plane position can lead to differences in geometry including varying coordination in the higher shells, relaxed volume, and other metrics of structural equivalence. As a result, some tolerance must be allowed to properly group structures.

Chemical stability for each binary compound was assessed by calculating the enthalpy of formation following the standard equation $\Delta H_f(XC) = H(XC) - H(C) - H(X)$, where $\Delta H_f(XC)$ is the enthalpy of formation per formula unit of different carbides, $H(C)$ is the enthalpy of elemental carbon in the graphite structure, and $H(X)$ is the enthalpy of the ground-state structure of $X=$ Si, Ge, Sn. The enthalpy of the binary compounds as well as elements was approximated by their total energies computed using the DFT-PBE exchange-correlation functional. The structures for the compounds used to calculate $\Delta H_f(XC)$ were relaxed using PBE, with the exception of graphite, which was relaxed using the opt86b-vdW DFT exchange correlation functional [60].

Phonon dispersions were calculated to evaluate the dynamical stability of all the high-symmetry structures for SiC, GeC, and SnC. For these calculations, we utilized Quantum Espresso [46–48]. All phonon calculations were performed with a Monkhorst-Pack k-point grid such that the number of k-points times the number of atoms is greater than or equal to 1000, and with a plane-wave energy cutoff of 816 eV. Phonon calculations were not completed for carbon. The PBE exchange correlation functional and PAW pseudopotentials were used for the phonon calculations. The electronic band structure calculations followed the same parameters. The k-point paths for phonon dispersions and electronic band structures were chosen based on previous work in Ref. [68].

The calculation methods for the input parameters to the BFOM equation were performed in VASP and follow those in Ref. [69]. Using the relaxed structures from the structure generator, the band gap and effective masses were taken from dense k-point electronic structure calculations at the GGA level. We used a dense k-point grid of $N \times nkpts = 8000$, where N is the number of atoms and $nkpts$ is the number of k-points. This paper uses a version of the semiempirical mobility model whose performance has been refined for n-type semiconductors in Ref. [50]. By computing the conduction band effective mass using gaussian smearing instead of the tetrahedron method, improved agreement with experiment is achieved for both effective mass and mobility. The bulk modulus was determined by fitting energy vs volume calculations to the Birch-Murnaghan equation of state. The phonon frequency and dielectric constant were obtained from density functional perturbation theory calculations using a plane wave energy cutoff of 520 eV and k-point grid density of $N \times nkpts = 1000$.

To get more accurate first-principles calculations of mobilities, electron-phonon coupling limited electron and hole mobilities for the zincblende structures of SiC, GeC, and SnC are computed using the iterative solution to the Boltzmann transport equation as implemented in the EPW code [41–45] of the Quantum Espresso suite [46–48]. Due to the absence of experimental data for GeC and SnC, we use structures relaxed in Quantum Espresso using the PBE exchange-correlation functional for all calculations. Norm-conserving pseudopotentials were generated using the ONCVPSP code [70] using the input files available at the PseudoDojo website [71]. In the electron-phonon calculations we use a plane-wave cutoff of 100 Ry for all materials. The coarse k-grid for the Wannier interpolation of the band structure was 16x16x16 for holes and 22x22x22 for electrons. This choice is informed by the coarse grids reported in Ref. [43]. The coarse q-grids were taken to be half of the k-grids. The fine k- and q-grids were taken to be 120x120x120 and computed using Wannier interpolation. The fine grids are solved using adaptive smearing as in Ref. [45]. When computing mobility with the fine grid, only states near the band edge will contribute, so for these calculations a small energy window around the band edge of 0.3 eV was found to be sufficient to converge the results. Maximally localized Wannier functions were selected as the basis for these calculations and computed using the wannier90 code [72,73]. The initial guess for the Wannier functions found to produce the smallest spread for both holes and electrons was found to be *sp3* hybridized orbitals centered on Si, Ge, and Sn for SiC, GeC, and SnC, respectively. Spin-orbit coupling effects, dipole-dipole, dipole-quadrupole, and quadrupole-quadrupole effects, and interpolation of velocity matrix elements includ-
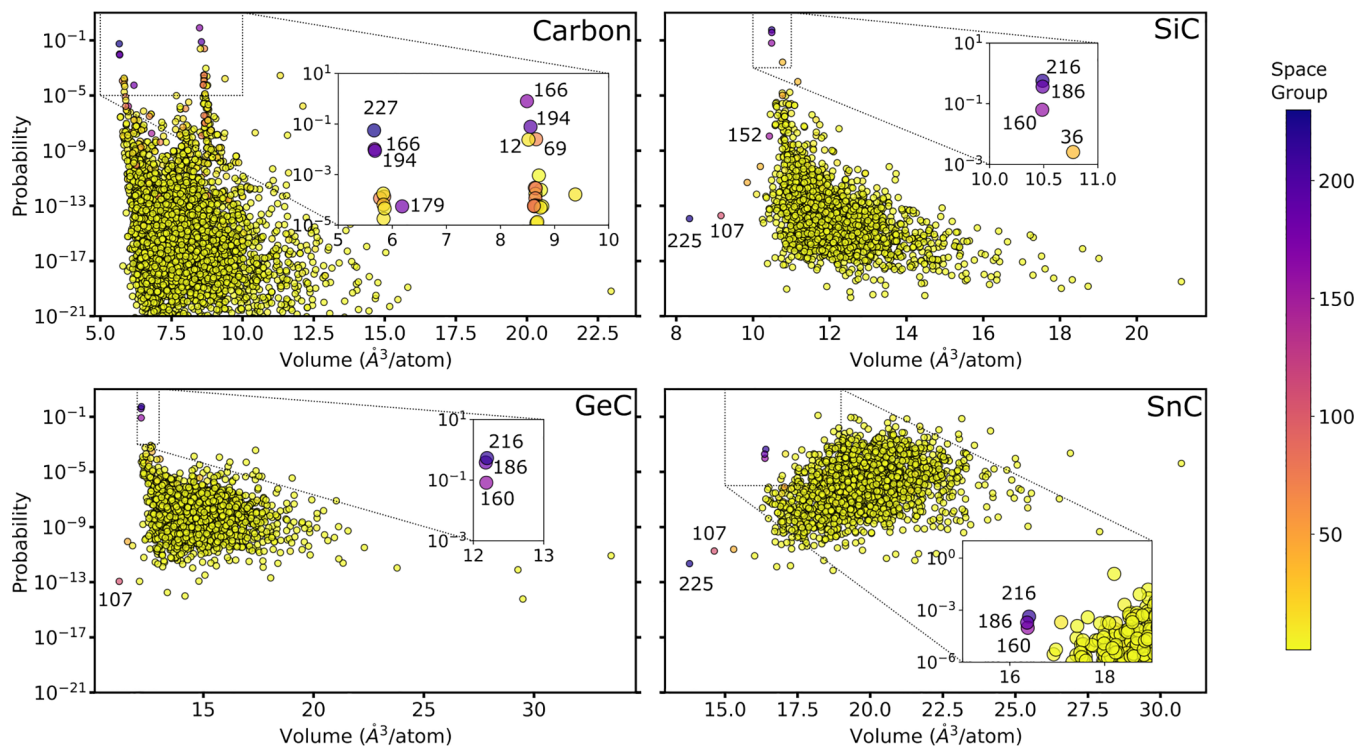
FIG. 3. Plots of the ensemble probabilities calculated using Eq. (2) at $T = 300$ K and $p = 0$ GPa vs the volume per atom for each of C, SiC, GeC, and SnC.

ing the correction for nonlocal potentials were all included [43,45,74]. Quadrupole tensors were computed using the ABINIT code [75–77] using norm-conserving pseudopotentials without a nonlinear core correction as required by ABINIT. These pseudopotentials were also generated using the ONCVPSP code [70]. The plane-wave energy cutoff was chosen to be 50 Ry (680 eV) and the k grids were chosen to be 12x12x12.

III. RESULTS

A. Ensemble probabilities

To identify polymorphs which are likely to be experimentally realizable, in Fig. 3 the ensemble probabilities computed according to Eq. (2) with $T = 300$ K and $p = 0$ GPa are plotted against the volume for each structure obtained by random sampling for each chemical composition. The most immediate features of these plots (with the exception of SnC) are "jets," narrow ranges of volume at which a number of structures are found with probabilities orders of magnitude greater than the rest of the sample. The probability plot for C has two distinct jets, one near 6 Å^3/atom and one near 9 Å^3/atom, while the plots for SiC and GeC each have one jet, located at 10.5 and 12 Å^3/atom, respectively.

The highest probability point on the C plot has s.g. #166 with a specific volume of 8.56 Å^3/atom. Its probability is 0.80. This structure is rhombohedral graphite as shown in Fig. 4. The structure with s.g. #194 in the same jet is hexagonal graphite, with a different stacking sequence, which has a probability of 0.08. Experimentally, rhombohedral graphite is found to have higher enthalpy than hexagonal graphite [78]. Previous DFT calculations have predicted rhombohedral
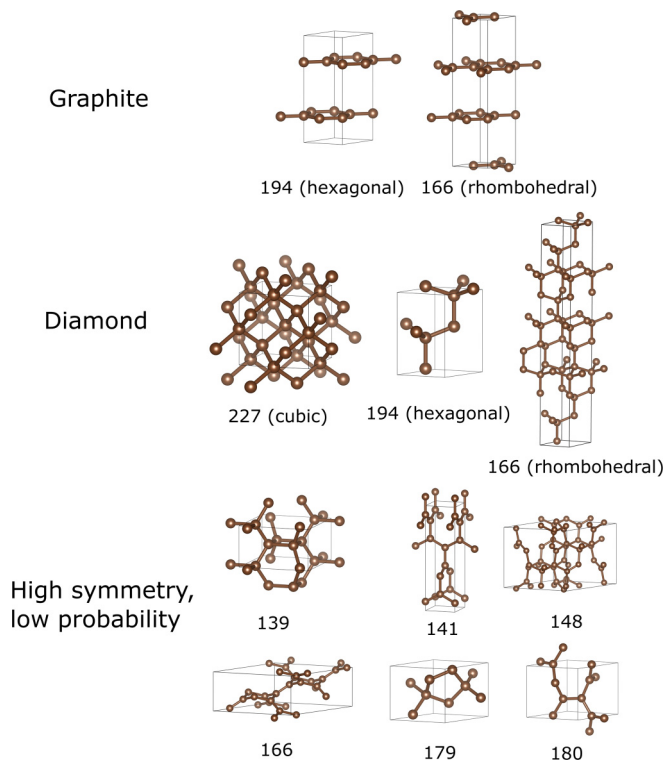

FIG. 4. The high-symmetry structures of carbon identified via random sampling. The known graphite and diamond structures are correctly identified to have high probability. A group of high-symmetry structures with lower probability is also identified. Some of these structures have previously been predicted computationally, but have not been realized.

graphite [79] to have 6 meV/atom lower total energy than hexagonal graphite. In this paper, using the vdW DFT functional by Klimeš [60] we find hexagonal graphite to have a 1 meV/atom lower total energy. However, the probability of rhombohedral graphite is predicted to be greater because it appears much more frequently (32 times in 4523 structures) as compared to the hexagonal structure (three times in 4523 structures) indicating a larger basin of attraction. Given the very small total energy differences and a small (or even nonexisting) kinetic barrier calculated in a later section, we expect transitions between these two graphite phases to be very fast at finite temperatures, and so we expect the rhombohedral phase to often relax to the hexagonal phase. Hence, it may even be appropriate to count these two structures as one larger basin instead of two smaller ones. This is consistent with experimental work that observes graphite at room temperature to be mostly hexagonal with some rhombohedral regions or stacking faults mixed in [80].

On the low-volume jet for carbon, the highest probability structure has s.g. #227 and a volume of 5.66 Å^3/atom, matching the structure of cubic diamond [81] with probability of 0.06. This jet also contains s.g. #194 near 6 Å^3/atom which is experimentally realized hexagonal diamond (lonsdaelite) [82]. Lonsdaelite's probability is 0.01. There is also a s.g. #166 at this volume, which is a rhombohedral diamond polytype which has been predicted, but not realized to our knowledge [83–86]. Its probability is 0.01. The structure with s.g. #139 in this jet has also been predicted computationally, but not realized to our knowledge [87,88]. This structure has a probability of 1.6×10^{-6}, suggesting that it would be much more challenging to realize experimentally. The jet also contains a structure with s.g. #179 that has not been discussed previously to our knowledge. This structure has 5-carbon rings and a symmetry distinct from other predicted or realized carbon structures, but has a probability of 5.5×10^{-5}, and so is also unlikely to be experimentally realizable. All of these structures are in shown in Fig. 4.

The only experimentally reported polymorph of carbon with space group number greater than 100 listed in the Inorganic Crystal Structure Database (ICSD) [89] that is not found via the random superlattice sampling method is a variant of graphite with s.g. #186 [90]. Subsequent analysis shows that this structure is very similar to the graphite with s.g. #194 with the only difference being the slight (on the order of ∼0.03 Å) buckling of the graphene sheets. Our DFT relaxations result in nearly complete removal of the buckling and the recovery of the symmetry consistent with the s.g. #194. All this confirms the *ab initio* random structure sampling is an effective strategy for identifying experimentally realizable polymorphs from first principles.

Note that some of the high-symmetry, low-probability structures identified by this method have low densities and form very open structures. This agrees with the observed diversity of low-density carbon structures that have been realized, such as buckminsterfullerene (which has a volume of 12.088 Å^3/atom) [91]. In particular, for the structure with a volume of approximately 12.12 Å^3/atom and a probability of 1.69×10^{-6}, all carbon atoms are threefold coordinated, forming 6-membered rings, which in turn form a network of large six-sided tubes. The structures with volumes greater than 15 Å^3/atom are characterized by networks consisting of structures with one to three edge-sharing rings that are bound to others by chains of four or more carbon atoms. The presence of these complex structures with large pores demonstrates the thoroughness with which the carbon phase space is sampled.

Moving to SiC, the jet in Fig. 3 contains three high-symmetry tetrahedrally-coordinated structures, with s.g. #s 216, 186, and 160. As already mentioned, the wurtzite (186) and rhombohedral (160) structure types are also known to form a range of polytypes, or structures with the same local coordination and close in symmetry but with a different stacking pattern in a particular direction (usually the c-axis) [89]. Interestingly, only the smallest possible polytype is found for the H (s.g. #186) structure type, that is, the 2H one, even though the 12-atom cell size should be large enough to accommodate the 6H polytype. We do not expect to find 4H because its 8-atom cell is incompatible with the 12-atom cell used in this study. If more random structures were calculated, we might expect to see 6H. In the case of the rhombohedral (R) structure types only the 9R structure with six atoms in the primitive unit cell is found whereas the experimentally realized ones (15R, 21R, and 24R) are incompatible with 12-atom cell and are not expected to appear in random sampling.

All three tetrahedrally coordinated structure types, namely the zincblende, wurtzite and rhombohedral, are observed experimentally in SiC [11]. Previous work has suggested that the 9R structure could be mischaracterized as 3C or 15R if only XRD is used to determine the crystal structure [92]. The ground-state zincblende structure (s.g. #216) has the highest probability (0.57) in the random sampling. This agrees with the experimentally observed ground state, evidenced by relaxation of s.g. #225 to s.g. #216 when pressure is released [19] and the observation that at high temperatures s.g. #216 reversibly converts to s.g. #186 [16]. The structures with s.g. #s 186 and 160 have probabilities of 0.37 and 0.06, respectively. The remaining experimentally observed structures of SiC have s.g. #s 225 [17,18] and 156 [89]. The rocksalt structure with s.g. #225 is found in the random sampling, with a very low probability (1.17×10^{-14} at 300 K and 0 GPa). When pressure is accounted for in the statistics to calculate the probabilities, s.g. #225 becomes the most likely structure at high pressure (probability close to 1 at 100 GPa). Space group 156 represents another sequence of the wurtzite derived (H) polytypes. They are labeled as 5H, 10H, 14H, and so on, and have unit cells with 10 atoms, 20 atoms, 28 atoms,..., respectively. While their sizes are incompatible with the 12-atom cells used in our search, their stacking sequences are combinations of two and three layer sequences [93–95] that are well represented by parent 2H and 9R structures found in the random sample.

The GeC jet contains the same three high-symmetry structures with s.g. #s, 216, 186, and 160, as in SiC. Experimental data for the structure of GeC is limited, as it has typically been grown either as an alloy with SiC or as a thin film [21–23,25]. The relative probabilities of each of these structures is similar to that found in SiC, with values of 0.53, 0.38, and 0.08 for s.g. #s 216, 186, and 160, respectively. The rocksalt structure with s.g. #225, which has been considered computationally in the literature, [12] does not appear at all in the random
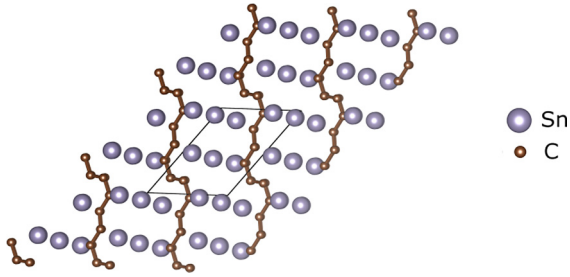
FIG. 5. The most probable structure of SnC. The Sn layers, which include atoms coordinated only to other Sn atoms, and the thin C layers clearly indicated that this structure has phase separated to the degree possible within a twelve-atom cell. This structure has a positive enthalpy of formation of 1.36 eV/formula unit.

sampling, which makes the GeC results qualitatively different than the SiC and SnC ones. Rocksalt (s.g. #225) GeC will be considered in later discussions for the sake of completeness. Note that two structures with probabilities of about 10^{-15} and volumes of approximately 57 and 173 Å^3/atom have been excluded from this plot to ensure visibility of the main features.

In case of SnC, the random structure sampling returns no obvious jet, although s.g. #s 216, 186, 160, and 225 all appear in the random sample for SnC. The high-symmetry structures have the same probability ordering, but at a lower total probability, with values of 4.26×10^{-4}, 1.91×10^{-4}, 9.6×10^{-5}, and 2.2×10^{-12} for s.g. #s 216, 186, 160, and 225, respectively. This family of high-symmetry structures will be explored in detail for each of the binary group-IV carbides in the following sections, and the absence of a jet can be explained by the significant chemical instability of SnC as discussed in the next section. The most likely structures for this chemistry show phase separated Sn and C in alternating layers as shown in Fig. 5. The probability of this structure is 0.12, and its volume is about 18 Å^3/atom. This structure has a positive enthalpy of formation of 1.36 eV/formula unit. High probability of this structure strongly suggests phase separation of SnC, even when the system is confined to a 12-atom unit cell with periodic boundary conditions.

Looking at broader trends in the distribution of structures across all four chemistries shown in Fig. 3, we note that almost all structures in the random sample have volumes greater than the tetrahedrally coordinated high-probability structures. For SiC, GeC, and SnC, the distributions are mainly to the right of the jet containing the zincblende structure, and for carbon to the right relative to the diamond structure. This skew of the distribution is exactly the opposite of what was found in Ref. [29] for Si, in which most of the structures have a volume less than the that of the ground-state diamond structure. This trend is shown to be physical, as liquid Si is known to be denser than the crystalline, diamond Si, while the opposite is true for carbon [96]. This suggests that the direction of skew of structures in terms of the density is related to the physical features of the potential energy surface and is not a bias of the method. Consequently, it can be inferred from our results that SiC, GeC, and SnC in the liquid form should all be less dense than their respective zincblende structures.

TABLE I. GGA calculated lattice constants of zincblende and wurtzite and formation enthalpy of zincblende SiC, GeC, and SnC. Experimental lattice constants for SiC in parentheses [15,20].

Compound	Zincblende a (Å)	Wurtzite a (Å)	c (Å)	ΔH_f (eV/f.u.)
SiC	4.38(4.36)	3.09(3.08)	5.07(5.05)	−0.45
GeC	4.60	3.25	5.34	0.82
SnC	5.08	3.59	5.87	1.57

To suggest ways that these compounds could be realized, note that the zincblende and wurtzite structures are often successfully grown as thin films on substrates with the same structure, such as AlAs on GaAs and ZnO on GaN [97,98]. The GGA calculated lattice constants of the carbides are presented in Table I. We compared the lattice constants to those of well known zincblende and wurtzite structured semiconductors and noted that zincblende GeC is within 1.5% of zincblende BP($a = 4.54$ Å) [99], wurtzite GeC is within 0.5% of ZnO ($a = 3.25$ Å) [100], and wurtzite SnC is within 1.2% (0.2%) of experimental (GGA) wurtzite InN ($a = 3.54$ Å in experiment [36], $a = 3.59$ Å calculated with GGA-PBE [35] as in the present paper). To our knowledge, SnC has not been experimentally realized, but the lattice constant match suggests that epitaxial growth of a thin film of the wurtzite phase on InN or on substrates used for InN may be an avenue for the first realization of this material.

B. Chemical and dynamical stability of the group-IV carbides

The enthalpy of formation for s.g. #216, the lowest energy high-symmetry DFT structure, for each of the binary group-IV carbides is listed in Table I. Only SiC is calculated to be chemically stable in DFT, while GeC and SnC are both predicted to decompose. SnC clearly phase separates when looking at the structure with the highest probability in the random sample, shown in Fig. 5. Contrary to SnC, the highest-probability structure for GeC has high symmetry, rather than being phase separated as predicted by the positive enthalpy of formation. This suggests that the high enthalpy of formation for SnC outweighs the interfacial energy created by phase separation in a 12-atom cell, but in GeC the interfacial penalties outweigh the energetic gain of phase separation. For any attempt to grow an epitaxial thin film of wurtzite SnC, we would expect this to require harsh synthesis conditions to overcome the very positive enthalpy of formation. We do note that there is some precedent in which monocarbides with enthalpies of formation comparable to SnC (0.68 eV/atom) have been reported experimentally in ReC (0.64 eV/atom) [79,101] and OsC (0.92 eV/atom) [79,102].

To analyze the possible existence of phonon instabilities in the high-symmetry structures (their dynamical stability) we calculated their phonon modes. Figure 6 shows phonon dispersions for each of the high-symmetry structures of each of the group-IV carbides. For s.g. #s 216, 186, and 160, all phonon modes are real, indicating that the system is dynamically stable for all three group-IV carbides. SiC and SnC both have real phonon modes and are therefore predicted to be dynamically stable in s.g. #225. In GeC, s.g. #225 has
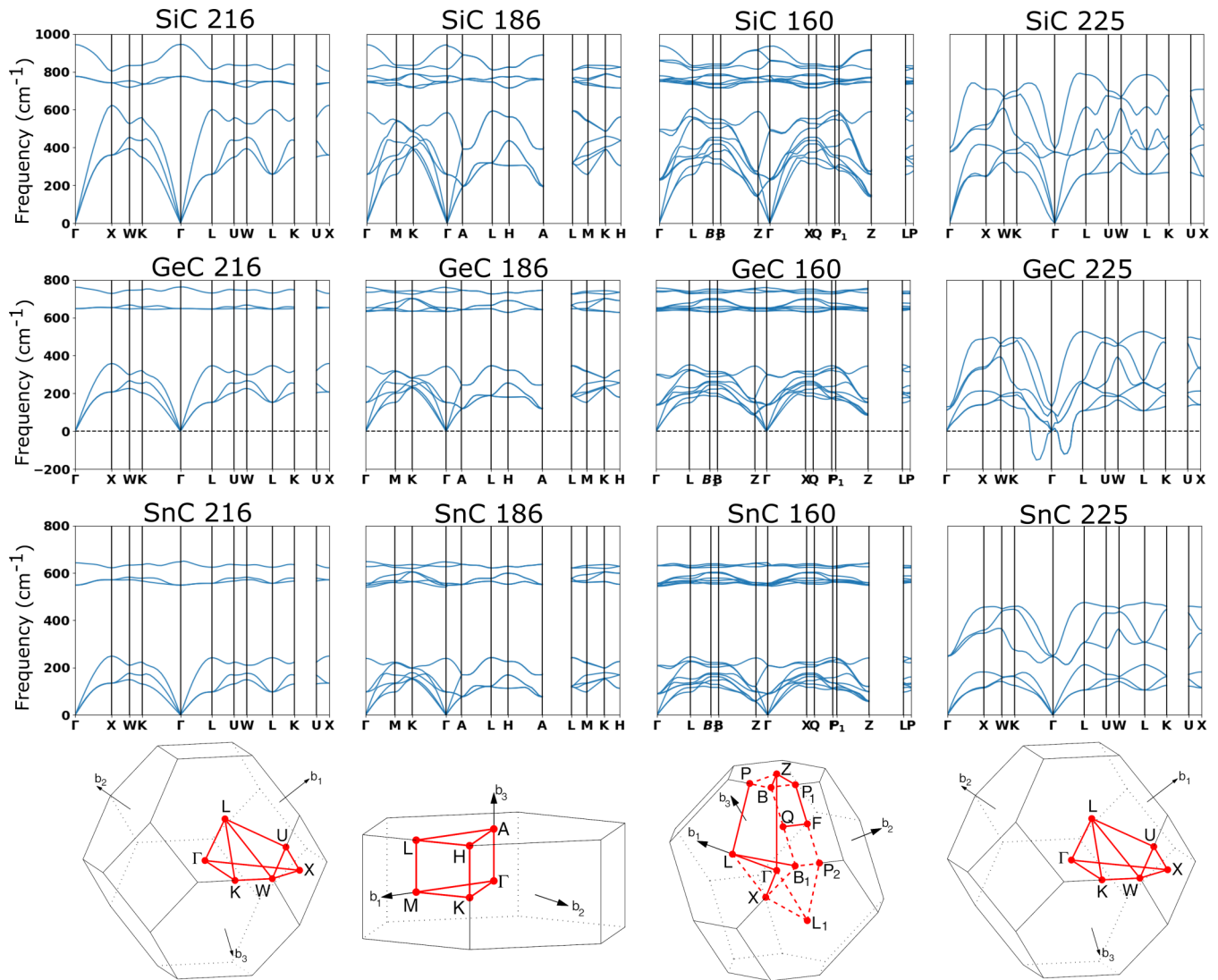
FIG. 6. Phonon dispersions of the high-symmetry structures of SiC, GeC, and SnC. All structures demonstrate dynamical stability with the exception of rocksalt GeC.

imaginary phonon modes between Γ and K and between Γ and L shown as negative values, indicating dynamical instability of this structure. This explains why rocksalt was not found by the *ab initio* random structure sampling. Indeed, by applying small random perturbations to the atomic positions of the conventional cell of rocksalt (s.g. #225) GeC we found it to relax spontaneously to the zincblende (s.g. #216) structure. Additionally, the movement of atoms for the imaginary mode between K and Γ is very similar to the movement of atoms from rocksalt (s.g. #225) to zincblende (s.g. #216) structures we found using our structure matching algorithm (see Sec. III C), matching this dynamical instability with this exact transition for GeC.

Otherwise, the phonon dispersions from Fig. 6 exhibit expected trends. By varying chemistry moving between rows in Fig. 6 one changes the mass contrast leading to the decrease in the phonon frequencies, with a greater decrease from SiC to GeC than from GeC to SnC following the trend in atomic masses of Si, Ge, and Sn. The softening of phonons present in both the acoustic and optical branches also agrees with

a corresponding decrease in bulk modulus computed by the Birch-Murnaghan equation of state [103,104].

Considering the influence of the structure on the dispersion, for a given chemistry the tetrahedrally coordinated structures all have approximately the same optical and acoustic frequency ranges with similar group velocities for most modes. The octahedrally coordinated s.g. #225 structures have decreased frequency in both acoustic and optical modes, with a more significant decrease in the optical frequencies. Between the Γ and K and between Γ and L, there is a softening of the optical modes for each of SiC, GeC, and SnC in the s.g. #225 structure. This softening is most pronounced in GeC, leading to the imaginary modes, which indicate dynamical instability, as discussed above.

Interestingly, the dynamical instability of sixfold coordinated rocksalt GeC is consistent with some observations of structural dependence on chemical trends. Dielectric theory, as proposed by Phillips [105], states that binary chemistries with a greater ionicity are more likely to have a sixfold coordinated ground-state structure, while binary structures with

less ionicity and more covalent character are more likely to be fourfold coordinated. Ge has greater electronegativity than Si or Sn, leading to less charge transfer to C (i.e., less ionicity) and a greater probability of GeC existing in a fourfold structure when compared to SiC or SnC.

C. Lifetime assessment (metastability) of high-symmetry structures

To estimate if these structures will be long-lived metastable states, optimal atom-to-atom maps and the associated changes in coordination between the relevant structures have been evaluated for each chemistry (C, SiC, GeC, and SnC) using the previously developed structure mapping algorithm implemented in the *pmpaths* code [33]. These maps are created by iterating through symmetry distinct unit-cell combinations and minimizing the change in coordination and the distance traveled by the atoms between the initial and final state. Previous work with this model shows that it correctly identifies structures that are likely to be long-lived relative to a ground-state structure by classifying the coordination (bonding) changes along the trajectories generated by the mapping as monotonic or nonmonotonic.

These approximations provide only a first-order estimate of whether or not a structure is likely to be a long-lived metastable state. A proper calculation of the mechanism and the barrier for transition between structures requires accounting for phenomena of nucleation and growth, which is beyond the scope of the present work. The barrier for growth of a center of new phase requires that the interface between phases be considered. The cofactor conditions described in Refs. [106,107] can be used determine the existence of an interface with conditions such that the strain penalty is minimized. Moreover, abandoning periodic boundary conditions in the structure mapping algorithm will also allow predictions of the interfacial (habit) plane and the orientation relationships between two phases [40].

A summary of the optimal atom-to-atom maps and the energetic penalty associated with change in coordination is shown in Fig. 7. Briefly, for the carbides, we find that transformations from s.g. #225 to any of the tetrahedrally coordinated structures are predicted to be rapid, while transformations from one tetrahedrally coordinated structure to another are expected to be sluggish, as in Fig. 7(a). For carbon, transformations between graphite phases are rapid, while graphite to diamond is slow and diamond to diamond is slow as in Fig. 7(b).

In Fig. 8, images of atomic positions, total energies along the pathways calculated statically (without any relaxations) and relative to the low-energy endpoint, and the first shell coordinations averaged over the atoms along these pathways are collected. The total energy along the trajectories represents an upper bound for the minimal energy profile because a calculation allowing these intermediate configurations to relax using the solid-state nudged elastic band method [108] would have energy less than or equal to the static snapshots. We find that the optimal atom-to-atom mapping reproduces known transformation mechanisms between zincblende (s.g. #216) and rocksalt (s.g. #225) and between wurtzite (s.g. #186) and rocksalt (s.g. #225) structures [33,39]. We have
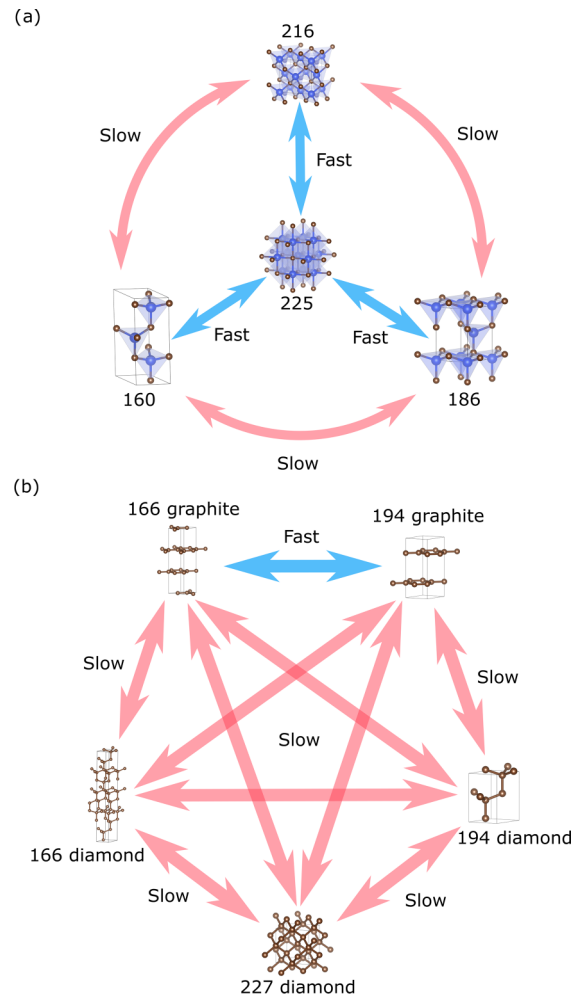

FIG. 7. A summary of the estimated transformation kinetics between the high-symmetry structures of (a) SiC, GeC, and SnC and (b) carbon.

also identified a pathway between s.g. #s 216 and 186 that breaks fewer bonds than a previously proposed pathway for this transformation [109]. The previously proposed pathway is specific to elevated pressure and finite temperature, and is similar to a pathway predicted in this paper moving from s.g. #186 through s.g. #225 to s.g. #216. Because our proposed pathway breaks fewer bonds, and because the upper bound of the energetic penalty for this direct transition is less than the lower bound of any pathway requiring the rocksalt structure as an intermediate step, we expect our pathway to be more descriptive of local processes occurring for this transition at ambient pressure. Beyond this, we predict new pathways from each of the s.g. #s 216, 186, and 225 to the rhombohedral (s.g. #160) structure, the 9R polytype. A previous pathway for the transformation from s.g. #186 (2H) to s.g. #160 (9R) requires the breaking of bonds between atoms in every layer [92], while our proposed pathway requires that bonds in only three out of six layers be broken. The s.g. #160 to s.g. #225 transition has not been previously studied to our knowledge. It is also predicted to be rapid.

We now describe the atomic pathways from s.g. #225 to each of the tetrahedrally coordinated structures as shown in
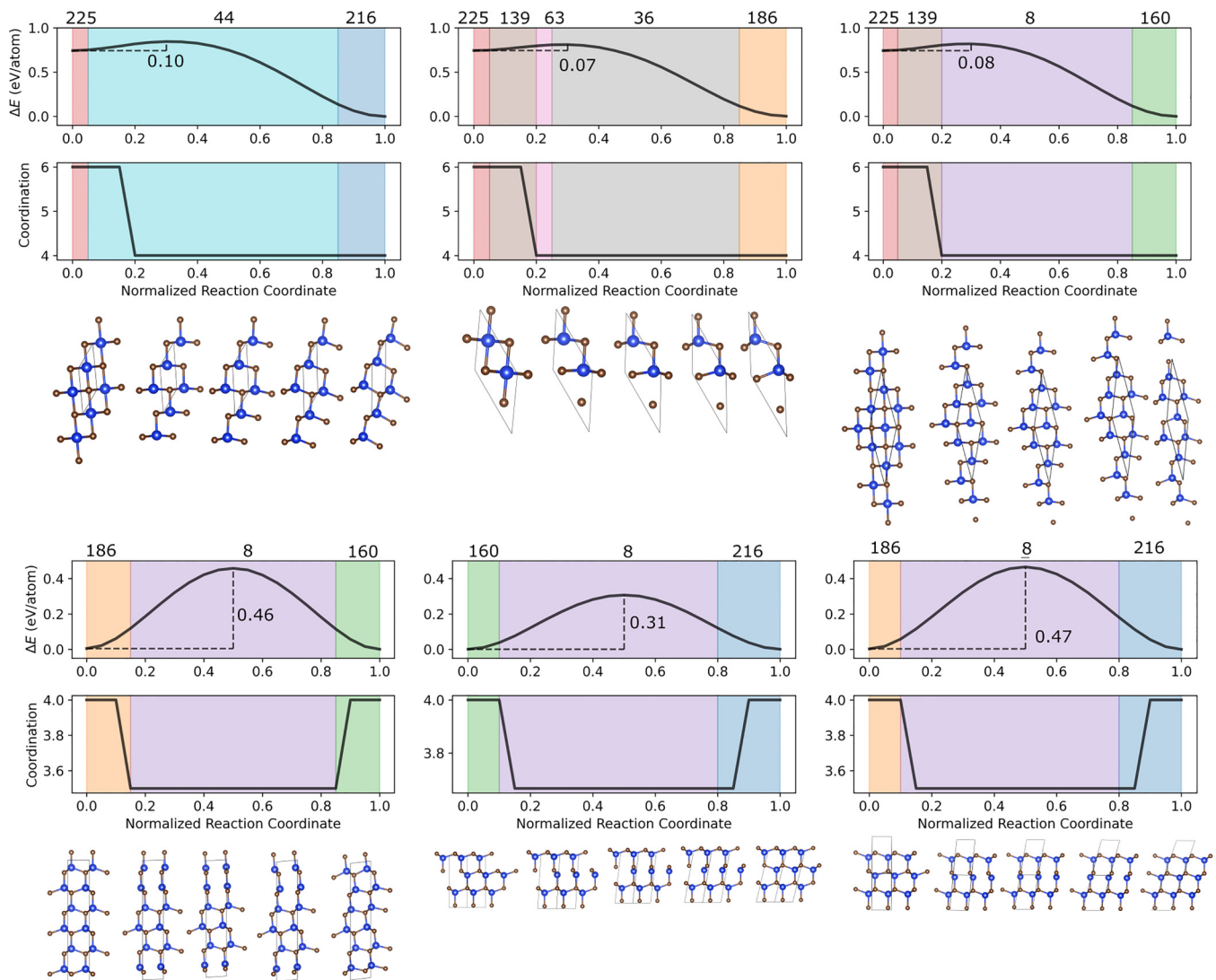
FIG. 8. Energy profiles, coordinations changes, and changes in crystal structure calculated statically along the transformation pathways for each optimal atom-to-atom map between the high-symmetry, high-probability structures of SiC. The colored regions in the plots are the regions along the pathway where the structure has the space group number indicated directly above that colored region.

the first row of Fig. 8. In the pathways from s.g. #225 to any of the tetrahedrally coordinated structures, the Si (Ge, Sn) atom moves away from two of its bonded carbon atoms, forming a seesaw structure. From there, the atom relaxes to the center of the tetrahedron. In the pathway from s.g. #225 to s.g. #216, from the angle in Fig. 8, all Si (Ge, Sn) atoms move up and to the left. This leads to an intermediate structure with s.g. #44. From s.g. #225 to s.g. #186, alternating rows of Si atoms move in opposing directions, with one row moving up and to the left and the other up and to the right. The resulting intermediate structures have s.g. #s 139, 63, and 36. Finally, in the pathway between s.g. #225 and s.g. #160, the repeating pattern is that two rows move up and to the left followed by one row moving up and to the right. A reduced symmetry is observed in the intermediate structures, with s.g. #139 followed by s.g. #8.

Given these pathways, we predict that the transformation between s.g. #225 and each of the other structures is rapid, as the coordination of all atoms decreases monotonically from six to four, and the predicted upper bound of the energetic

penalty associated with change in coordination is small (less than 0.1 eV). This agrees with the experimental observation that when pressure is released from s.g. #225 silicon carbide, it will transition to a low-pressure phase [17–19]. At room temperature, the measured transition pressure of 100 GPa from s.g. #216 to s.g. #225 for SiC greatly exceeds the theoretical equilibrium pressure of approximately 60 GPa [19]. By computing the same energetic penalties due to coordination in terms of enthalpy, $H = U + PV$, we can approximately reproduce the room temperature hysteresis just from the energy profiles shown in Fig. 8. That is, a low barrier for transition from tetrahedral to octahedral occurs well above the equilibrium pressure and a low barrier for transition from octahedral to tetrahedral occurs well below the equilibrium pressure [17,18].

In contrast, the pathways between s.g. #s 216 and 186, between s.g. #s 216 and 160, and between s.g. #s 186 and 160 all involve the inversion of a tetrahedron in the structure, and therefore a reduction of the number of bonds per atom

to three for some atoms in the structure, as seen in the first row of Fig. 8. This is less than the number of bonds in the endpoint structures, suggesting that these transformations are slow according to the coordination-based model of polymorph lifetime [33]. All of the pathways between the three structures, which have high probability at ambient pressure are slow, suggesting that any of these three structures will have a long lifetime at ambient conditions if realized. The upper bound estimate of the energetic penalty associated with change in coordination supports this conclusion. This agrees with the observation of s.g. #s 216, 186, and 160 as long-lived phases of SiC in experiment [11].

The same process is repeated for the high-probability structures of carbon, with a summary of the results collected in Fig. 7(b). Images of atomic pathways, total energies relative to the low-energy endpoint, and coordinations of the structures along these pathways are collected in Fig. S2 of the Supplemental Material [54]. The only pathway classified as fast is between the two different graphite structures, which have no coordination change, and a very small barrier. This is what we would expect physically, because the weak van der Waals interactions between layers should permit them to rapidly change position with respect to one another. All pathways between diamond structures require the inversion of a tetrahedron, nonmonotonic variation in coordination, and a corresponding large energetic penalty associated with change in coordination. Pathways between graphite and diamond require that graphene sheets buckle and bond with the neighboring sheets. Though these pathways have a monotonic change in coordination, they are still slow transformations because the buckling of the graphene sheets involves the breaking of π bonds, and so the total change in bonding is not monotonic, as noted in Ref. [33]. We note that the transformation from graphite with s.g. #194 to diamond with s.g. #166 has an exceptionally high energetic penalty associated with coordination, and a slightly stranger pathway. If the structure were to convert from hexagonal to rhombohedral graphite, and then to rhombohedral diamond, the energetic penalty associated with change in coordination would be much lower. Cases such as this, which have an intermediate structure that lowers the barrier may be a limitation of the framework used in this manuscript and defined in Ref. [33], which relies on minimizing the direct distance that the atoms must move between the initial and final structures. This can be remedied by having a complete set of structures with likely intermediates included, as in the alternate pathway defined in the text above.

D. Electronic structure and related properties of high-symmetry structures

Electronic structures for s.g. #s 216, 186, 160, and 225 of SiC, GeC, and SnC are collected in Fig. 9. When studying the band structures from Fig. 9, a few patterns are immediately apparent. Structures with s.g. #s 216, 186, and 160 exhibit a finite band gap. The energy of the first conduction band at the Γ-point decreases as chemistry changes from SiC to GeC to SnC. This changes the nature of the band gap from indirect in SiC and GeC into a direct gap in SnC for all of these three structures. The magnitude of the band gap changes as well. SnC has a gap more than 1 eV smaller than those of GeC and

SiC, which have gaps of a similar magnitude. The conduction band minimum at Γ for SnC is also much more dispersive than the conduction band minima at X in SiC and GeC, leading to a much lower effective mass and greater predicted electron mobility in SnC than in the other two carbides.

Looking across different rows in Fig. 9, that is, as structure varies for a fixed chemistry, there are also immediate trends. Band gap increases when going from the zincblende (s.g. #216) to wurtzite (s.g. #186) and rhombohedral structures (s.g. #160), but much more so for SiC and GeC than in the case of SnC. For the former two the gap goes from 1.38 eV and 1.65 eV, respectively, in the zincblende structure to more than 2 eV in the other two structures. This trend is less pronounced for SnC. We acknowledge the systematic underestimate of the band gap when calculating electronic structure with GGA, but the trends are expected to be approximately the same [111]. In contrast, all the rocksalt structures for each of SiC, GeC, and SnC exhibit a negative band-gap. The conduction band minima at the X-point are lower in energy than the tops of the respective valence bands, all along the Γ-K direction. Again, going from Si to Ge to Sn, this effect becomes more pronounced.

Additionally, electronic and transport properties relevant for power electronics performance as described by the low-frequency Baliga figure of merit (BFOM) [51] are listed in Table II. The interest in analyzing the propensity of various structures for power applications stems from SiC, a known power electronics material that is increasingly being used as an alternative to Si-based devices. Also, elemental carbon in the diamond structure is a well-known wide gap semiconductor material, which correlates to a large theoretical breakdown field and therefore a large BFOM.

Trends in transport properties found using the semiempirical model agree with experiment [110] to within half an order of magnitude. While admittedly large, deviations of this magnitude are typically observed between different experiments on seemingly very similar samples, and the model that is fit to existing experimental data cannot be expected to perform better than the training data itself. That said, our model finds the order of magnitude and the mobility trends between different SiC structures to be in agreement with experiments as shown in Table II, with relatively high mobility in the 3C and 4H structures and lower mobility in the 2H, 6H, and 15R polymorphs.

To validate the model mobilities, we compute from first principles the electron and hole mobilities of the s.g. # 216 structures for each of SiC, GeC, and SnC using the EPW code. The resulting drift and Hall mobilities computed at temperatures ranging from 150 to 500 K are shown in Fig. 10. We note that the computed electron mobility at room temperature of SiC is about a factor of 2 greater than that reported in experiments [110]. Poncé *et al.* [43] state that there remains an open question regarding whether the use of hybrid functionals, or many body perturbation theory, or going beyond the Boltzmann transport formalism will lead to better agreement with experiment. They also observe that, for SiC in particular, this overestimation persists when replacing the GGA effective mass and dielectric constants with experimental values [43], indicating that higher mobility may be a real possibility in this material rather than a computational artifact. With this in
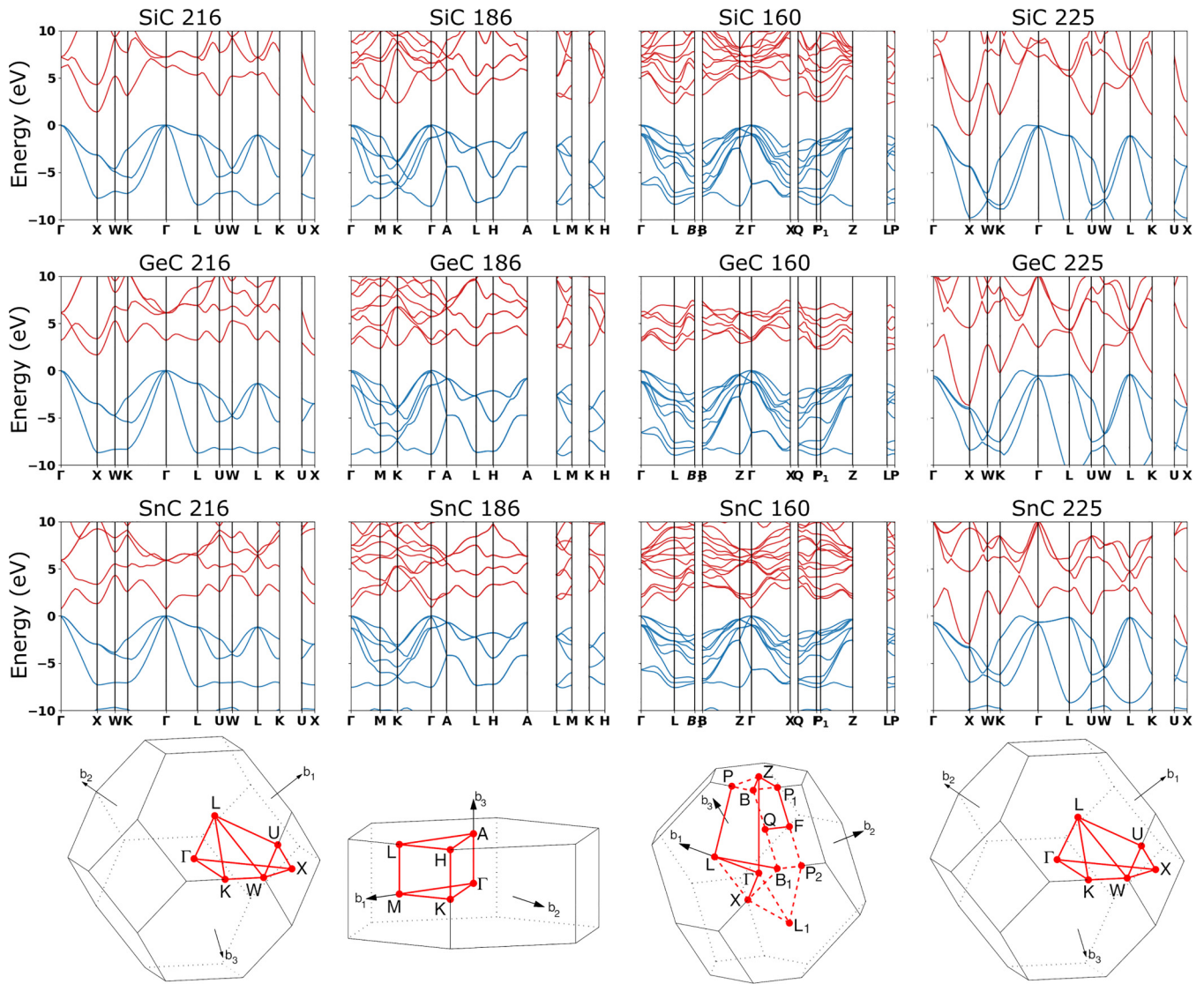
FIG. 9. Electronic band structures of the high-symmetry structures of SiC, GeC, and SnC.

mind, the computed electron mobility of SnC is exceptional (17 304 cm^2/Vs), an order of magnitude greater than that of SiC.

We propose that the high electron mobility of 3C-SnC compared to 3C-SiC and 3C-GeC is a consequence of the highly dispersive conduction band minimum, which in SnC is located at the Gamma-point contrary to 3C-SiC and 3C-GeC, which have their conduction band minima at the X-point. While the large enthalpy of formation of SnC suggests that synthesis may be difficult, such a promising property may warrant attempts to make this material, such as epitaxial thin-film growth of the wurtzite phase on the closely lattice-matched wurtzite InN as noted at the end of Sec. III A.

GeC is predicted to have lower mobility than SiC. This is expected because GeC has overall lower-frequency phonons than SiC, leading to enhanced scattering. While SnC has even lower-frequency phonons, the decrease in effective mass due to the dispersive conduction band minimum outweighs this effect.

The estimated *n*-type BFOM for SiC and GeC for all structures is significantly larger than *n*-type Si. For SnC, the *n*-type

BFOM is increased to the point that it outperforms silicon due to the exceptional electron mobility mentioned above, but its realistic application is likely limited by the difficulty in synthesizing SnC, and its small estimated band gap. The only group of BFOM values which performs worse than *n*-type Si in this family is the *p*-type BFOM for SnC.

Fixing chemistry and varying structure, the band gap of s.g. #186 is greater than that for s.g. #160, with the smallest gap for s.g. #216, and a negative gap for s.g. #225. The negative gap is reported in the table as a zero gap, as it should lead to metallic behavior, and therefore there is no BFOM for these chemistries in s.g. #225. As expected, the breakdown field follows the same trend as the band gap. This is because avalanche breakdown requires that electrons in the conduction band accelerated by the electric field excite valence electrons across the band gap.

IV. CONCLUSIONS

We identify a common family of metastable tetrahedrally coordinated polymorphs with s.g. #s 216, 186, and 160 for

TABLE II. Calculated electronic properties relevant for power electronics applications for all of the studied group-IV carbides and their structures. DFT calculated band gaps (E_g^{DFT}), experimental electron mobilities at room temperature for single crystals where available from Ref. [110] (μ_n^{expt}), electron and hole mobilities calculated with first principles electron-phonon coupling for s.g. # 216 (μ_n^{EPW}, μ_p^{EPW}), and semi-empirically modeled mobilities of electrons (μ_n^{model}), calculated dielectric constant (ε), modeled electric breakdown fields (E_b), and power electronics Baliga figure of merit (BFOM) for the assumed n-type doped materials expressed relative to the value calculated for n-type crystalline Si. *The 4H polymorph is included in this table as a reference because of its widespread use in power electronics applications and 6H and 15R are included for completeness.

| Compound /s.g. #	E_g^{DFT} (eV)	μ_p^{EPW} (cm²/Vs)	μ_n^{expt}	μ_n^{EPW}	μ_n^{model}	ε	E_b (MV/cm)	BFOM p-type (EPW) relative to Si-n	BFOM n-type (EPW)	BFOM n-type (model)
SiC/216 (3C)	1.38	71	25-750	1813	2339	10.22	1.47	1.12	29	37
SiC/186 (2H)	2.37				215	10.44	2.73			22
SiC/186 (4H)*	2.23		600-950		2191	10.4	2.84			252
SiC/186 (6H)*	2.04		20-500		287	10.6	2.63			27
SiC/160 (9R)	2.26				113	10.27	2.73			11
SiC/160 (15R)*	1.96		400		90	10.58	2.47			7
SiC/225	0.00									
GeC/216 (3C)	1.65	245		543	1460	11.01	1.46	4.07	9	24
GeC/186 (2H)	2.37				103	10.97	2.39			7
GeC/186 (4H)	2.16				390	11.03	2.21			22
GeC/160 (9R)	2.13				83	10.81	2.15	14.5		4
GeC/225	0.00									
SnC/216 (3C)	0.66	291		17304	2212	14.10	0.68	0.63	37	5
SnC/186 (2H)	0.84				2572	13.59	0.85			10
SnC/186 (4H)	0.82				1520	13.86	0.85			6
SnC/160 (9R)	0.77				1969	13.45	0.81			7
SnC/225	0.00									
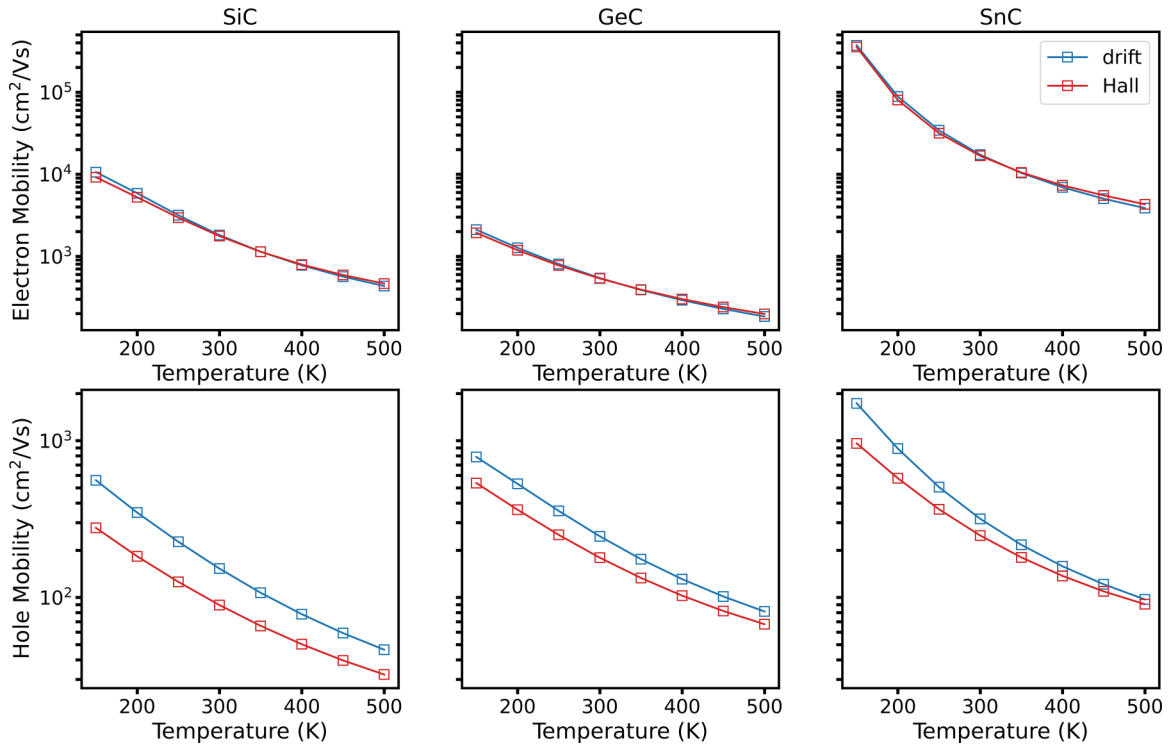
FIG. 10. Drift and Hall mobilities of electrons and holes computed using the iterative Boltzmann transport equation with scattering rates informed by first-principles electron-phonon coupling constants at the GGA level for SiC, GeC, and SnC.

the group-IV carbides (XC, $X =$ Si, Ge, Sn) by using the *ab initio* random sampling approach. This set of structures is in good agreement with the family of polymorphs experimentally known for SiC. We also find the polymorphs of carbon known to be experimentally realized as bulk crystals and a new high-density structure of carbon with s.g. #179. The rock salt structure with s.g. #225 is identified and found to be dynamically stable in both SiC and SnC, while it is dynamically unstable and therefore not found by random sampling in GeC. Dynamical stability and transformation pathway models agree with the long lifetime of tetrahedrally coordinated SiC phases and the relaxation of rocksalt to tetrahedrally coordinated structures when pressure is released. These models also suggest long lifetimes for tetrahedrally coordinated GeC and SnC polymorphs. Each of the tetrahedrally coordinated structures of the group-IV carbides is estimated to have an *n*- and *p*-type BFOM for power electronics, which exceeds that of silicon. The s.g. # 216 structure of SnC has been predicted to exhibit exceptionally high electron mobility using first-principles electron-phonon coupling calculations and the iterative solution to the Boltzmann transport equation. While SnC is unstable with respect to chemical decomposition, the lattice match between wurtzite SnC and wurtzite InN suggests a possible avenue for the epitaxial growth of thin films of wurtzite SnC. The significant variation in electronic properties among different crystal structures for each of the group-IV carbides reinforces the advantages of searching for novel functional materials in the space of metastable materials.

[1] A. R. Oganov, C. J. Pickard, Q. Zhu, and R. J. Needs, Structure prediction drives materials discovery, Nat. Rev. Mater. **4**, 331 (2019).

[2] S. Curtarolo, G. L. Hart, M. B. Nardelli, N. Mingo, S. Sanvito, and O. Levy, The high-throughput highway to computational materials design, Nat. Mater. **12**, 191 (2013).

[3] W. Sun, C. J. Bartel, E. Arca, S. R. Bauers, B. Matthews, B. O. nanos, B.-R. Chen, M. F. Toney, L. T. Schelhas, W. Tumas *et al.*, A map of the inorganic ternary metal nitrides, Nat. Mater. **18**, 732 (2019).

[4] C. Collins, M. S. Dyer, M. J. Pitcher, G. F. S. Whitehead, M. Zanella, P. Mandral, J. B. Claridge, G. R. Darling, and M. J. Rosseinsky, Accelerated discovery of two crystal structure types in a complex inorganic phase field, Nature (London) **546**, 280 (2017).

[5] R. Gautier, X. Zhang, L. Hu, L. Yu, Y. Lin, T. O. Sunde, D. Chon, K. R. Poeppelmeier, and A. Zunger, Prediction and accelerated laboratory discovery of perviously unknown 18-electron ABX compounds, Nat. Chem. **7**, 308 (2015).

[6] C. J. Pickard and R. J. Needs, *Ab initio* random structure searching, J. Phys.: Condens. Matter **23**, 053201 (2011).

[7] S. Botti, J. A. Flores-Livas, M. Amsler, S. Goedecker, and M. A. L. Marques, Low-energy silicon allotropes with strong absorption in the visible for photovoltaic applications, Phys. Rev. B **86**, 121204(R) (2012).

[8] F. Therrien, E. B. Jones, and V. Stevanović, Metastable materials discovery in the age of large-scale computation, Appl. Phys. Rev. **8**, 031310 (2021).

[9] A. Mujica, A. Rubio, A. Muñoz, and R. J. Needs, High-pressure phases of group-IV, II-V, and II-VI compounds, Rev. Mod. Phys. **75**, 863 (2003).

[10] M. J. Mehl, M. Ronquillo, D. Hicks, M. Esters, C. Oses, R. Friedrich, A. Smolyanyuk, E. Gossett, D. Finkenstadt, and S. Curtarolo, Tin-pest problem as a test of density functionals using high-throughput calculations, Phys. Rev. Mater. **5**, 083608 (2021).

[11] L. S. Ramsdell, Studies on silicon carbide, Am. Mineral. **32**, 64 (1947).

[12] A. Hao, X. Yang, X. Wang, Y. Zhu, X. Liu, and R. Liu, First-principles investigations on electronic, elastic and optical properties of XC (X = Si, Ge, and Sn) under high pressure, J. Appl. Phys. **108**, 063531 (2010).

[13] R. Pandey, M. Rérat, C. Darrigan, and M. Causa, A theoretical study of stability, electronic, and optical properties of GeC and SnC, J. Appl. Phys. **88**, 6462 (2000).

[14] J. B. Varley, B. Shen, and M. Higashiwaki, Wide bandgap semiconductor materials and devices, J. Appl. Phys. **131**, 230401 (2022).

[15] J. Serrano, J. Strempfer, M. Cardona, M. Schwoerer-Böhning, H. Requardt, M. Lorenzen, B. Stojetz, P. Pavone, and W. J. Choyke, Determination of the phonon dispersion of zinc blende (3C) silicon carbide by inelastic x-ray scattering, Appl. Phys. Lett. **80**, 4360 (2002).

[16] L. B. Griffiths, Defect structure and polytypism in silicon carbide, J. Phys. Chem. Solids **27**, 257 (1966).

[17] M. Yoshida, A. Onodera, M. Ueno, K. Takemura, and O. Shimomura, Pressure-induced phase transition in SiC, Phys. Rev. B **48**, 10587 (1993).

[18] K. Daviau and K. K. M. Lee, Zinc-blende to rocksalt transition in SiC in a laser-heated diamond-anvil cell, Phys. Rev. B **95**, 134108 (2017).

[19] K. Daviau and K. K. Lee, High-pressure, high-temperature behavior of silicon carbide: A review, Crystals **8**, 217 (2018).

[20] K. M. Merz and R. F. Adamsky, Synthesis of the wurtzite form of silicon carbide, J. Am. Chem. Soc. **81**, 250 (1959).

[21] N. Gupta, B. P. Veetil, H. Xia, S. K. Karuturi, G. Conibeer, and S. Shrestha, Synthesis of nano-crystalline germanium carbide using radio frequency magnetron sputtering, Thin Solid Films **592**, 162 (2015).

[22] D. C. Booth and K. J. Voss, The optical and structural properties of CVD germanium carbide, J. Phys. Colloq. **42**, C4-1033 (1981).

[23] J. T. Harrold and V. L. Dalal, Growth and properties of crystalline germanium-carbide alloys using electron cyclotron resonance plasma processing, J. Non-Cryst. Solids **270**, 255 (2000).

[24] J. Huguenin-Love, R. Soukup, N. Ianno, J. Schrader, D. Thompson, and V. Dalal, Optical and cyrstallographic analysis of thin films of GeC deposited using a unique hollow cathode sputtering technique, Mater. Sci. Semicond. **9**, 759 (2006).

[25] J. Kouvetakis, M. Todd, D. Chandrasekhar, and D. J. Smith, Novel chemical routes to silicon-germanium-carbon materials, Appl. Phys. Lett. **65**, 2960 (1994).

[26] M. Konagai, S. Miyajima, Y. Yashiki, T. Watahiki, K. L. Narayanan, and A. Yamamada, Progress in the development of microcrystalline 3C-SiC, SiGeC and GeC thin films for solar cell applications, Conf. Rec. IEEE Photovolt. Spec. Conf., 1424 (2005).

[27] V. Stevanović, Sampling Polymorphs of Ionic Solids using Random Superlattices, Phys. Rev. Lett. **116**, 075503 (2016).

[28] P. Hohenberg and W. Kohn, Inhomogeneous electron gas, Phys. Rev. **136**, B864 (1964).

[29] E. B. Jones and V. Stevanović, Polymorphism in elemental silicon: probabilistic interpretation of the realizability of metastable structure., Phys. Rev. B **96**, 184101 (2017).

[30] C. M. Caskey, A. Holder, S. Shulda, S. Christensen, D. Diercks, C. Schwartz, D. Biagioni, D. Nordlund, A. Kukliansky, A. Natan *et al.*, Synthesis of a mixed-valent tin nitride and considerations of its possible crystal structures, J. Chem. Phys. **144**, 144201 (2016).

[31] E. B. Jones and V. Stevanović, The glassy solid as a statistical ensemble of crystalline microstates, npj Comput. Mater. **6**, 56 (2020).

[32] R. Woods-Robinson, V. Stevanovic, S. Lany, K. N. Heinselman, M. K. Horton, K. A. Persson, and A. Zakutayev, Role of disorder in the synthesis of metastable zinc zirconium nitrides, Phys. Rev. Mater. **6**, 043804 (2022).

[33] V. Stevanović, R. Trottier, C. Musgrave, F. Therrien, A. Holder, and P. Graf, Predicting kinetics of polymorphic transformations from structure mapping and coordination analysis, Phys. Rev. Mater. **2**, 033802 (2018).

[34] F. Therrien, P. Graf, and V. Stevanović, Matching crystal structures atom-to-atom, J. Chem. Phys. **152**, 074106 (2020).

[35] F. Litimein, B. Bouhafs, G. Nouet, and P. Ruterana, Meta-GGA calculation of the electronic structure of group III-V nitrides, Phys. Status solidi B **243**, 1577 (2003).

[36] V. Y. Davydov, A. A. Klochikhin, R. P. Seisyan, V. V. Emtsev, S. V. Ivanov, F. Bechstedt, J. Furthmüller, H. Harima, A. Mudryi, J. Alderhoold, and O. Semchinova, Absorption and emission of hexagonal InN. Evidence of narrow fundamental band gap, Phys. Status Solidi B **229**, r1 (2002).

[37] G. L. Zhao and D. Bagayoko, Electronic structure and charge transfer in 3C- and 4H-SiC., New J. Phys. **2**, 16 (2000).

[38] M. Aykol, S. S. Dwaraknath, W. Sun, and K. A. Persson, Thermodynamic limit for synthesis of metastable inorganic materials, Sci. Adv. **4**, eaaq0148 (2018).

[39] C. Capillas, J. M. Perez-Mato, and M. I. Aroyo, Maximal symmetry transition paths for reconstructive phase transitions, J. Phys.: Condens. Matter **19**, 275203 (2007).

[40] F. Therrien and V. Stevanović, Minimization of Atomic Displacements as a Guiding Principle of the Martensitic Phase Transformation, Phys. Rev. Lett. **125**, 125502 (2020).

[41] F. Giustino, M. L. Cohen, and S. G. Louie, Electron-phonon interaction using Wannier functions, Phys. Rev. B **76**, 165108 (2007).

[42] S. Poncé, E. Margine, C. Verdi, and F. Giustino, EPW: Electron–phonon coupling, transport and superconducting properties using maximally localized Wannier functions, Comput. Phys. Commun. **209**, 116 (2016).

[43] S. Poncé, F. Macheda, E. R. Margine, N. Marzari, N. Bonini, and F. Giustino, First-principles predictions of Hall and drift mobilities in semiconductors, Phys. Rev. Res. **3**, 043022 (2021).

[44] S. Poncé, E. R. Margine, and F. Giustino, Towards predictive many-body calculations of phonon-limited carrier mobilities in semiconductors, Phys. Rev. B **97**, 121201(R) (2018).

[45] F. Macheda and N. Bonini, Magnetotransport phenomena in *p*-doped diamond from first principles, Phys. Rev. B **98**, 201201(R) (2018).

[46] P. Gianozzi, S. Baroni, N. Bonini, M. Calandra, R. Car, C. Cavazzoni, D. Ceresoli, G. L. Chiarotti, M. Cococcioni, and I. Dabo, QUANTUM ESPRESSO: A modular and open-source software project for quantum simulations of materials, J. Phys.: Condens. Matter **21**, 395502 (2009).

[47] P. Giannozzi, O. Andreussi, T. Brumme, O. Bunau, M. B. Nardelli, M. Calandra, R. Car, C. Cavazzoni, D. Ceresoli, M. Cococcioni, and N. Colonna, Advanced capabilities for materials modelling with QUANTUM ESPRESSO, J. Phys.: Condens. Matter **29**, 465901 (2017).

[48] P. Giannozzi, O. Baseggio, P. Bonfà, D. Brunato, R. Car, I. Carnimeo, C. Cavazzoni, S. D. Gironcooli, P. Delugas, F. F. Ruffino, and A. Ferretti, QUANTUM ESPRESSO toward the exascale, J. Chem. Phys. **152**, 154105 (2020).

[49] J. Yan, P. Gorai, B. Ortiz, S. Miller, S. A. Barnett, T. Mason, V. Stevanovic, and E. S. Toberer, Material descriptors for predicting thermoelectric performance, Energy Environ. Sci. **8**, 983 (2015).

[50] E. M. Garrity, C.-W. Lee, P. Gorai, M. B. Tellekamp, A. Zakutayev, and V. Stevanović, Computational identification of ternary wide-band-gap oxides for high-power electronics, PRX Energy **1**, 033006 (2022).

[51] B. J. Baliga, Semiconductors for high-voltage, vertical channel field-effect transistors, J. Appl. Phys. **53**, 1759 (1982).

[52] Y. Sun, S. A. Boggs, and R. Ramprasad, The intrinsic electrical breakdown strength of insulators from first principles, Appl. Phys. Lett. **101**, 132906 (2012).

[53] C. Kim, G. Pilania, and R. Ramprasad, From organized high-throughput data to the phenomenological theory using machine learning: The example of dielectric breakdown, Chem. Mater. **28**, 1304 (2016).

[54] See Supplemental Material at http://link.aps.org/supplemental/10.1103/PhysRevMaterials.7.053606 for convergence plots, carbon pathway details, structures, and mobility calculation inputs.

[55] G. Kresse and J. Hafner, *Ab initio* molecular dynamics for liquid metals, Phys. Rev. B **47**, 558 (1993).

[56] G. Kresse and J. Hafner, *Ab initio* molecular dynamics simulation of the liquid-metal-amorphous-semiconductor transition in germanium, Phys. Rev. B **49**, 14251 (1994).

[57] G. Kresse and J. Furthmüller, Efficient iterative schemes for *ab initio* total-energy calculations using a plane-wave basis set, Phys. Rev. B **54**, 11169 (1996).

[58] G. Kresse and J. Furthmüller, Efficiency of *ab-initio* total energy calculations for metals and semiconductors using a plane-wave basis set, Comput. Mater. Sci. **6**, 15 (1996).

[59] W. H. Press, S. A. Teukolsky, W. T. Vetterling, and B. P. Flannery, *Numerical Recipes 3rd Edition: The Art of Scientific Computing* (Cambridge University Press, New York, 1989).

[60] J. Klimeš, D. R. Bowler, and A. Michaelides, van der Waals density functionals applied to solids, Phys. Rev. B **83**, 195131 (2011).

[61] J. Klimeš, D. R. Bowler, and A. Michaelides, Chemical accuracy for the van der Waals density functional, J. Phys.: Condens. Matter **22**, 022201 (2009).

[62] Z. Wang, S. M. Selbach, and T. Grande, van der Waals density functional study of the energetics of alkali metal intercalation in graphite, RSC Adv. **4**, 4069 (2014).

[63] H. Moriwake, A. Kuwabara, C. A. Fisher, and Y. Ikuhara, Why is sodium-intercalated graphite unstable?, RSC Adv. **7**, 36550 (2017).

[64] J. P. Perdew, K. Burke, and M. Ernzerhof, Generalized Gradient Approximation Made Simple, Phys. Rev. Lett. **77**, 3865 (1996).

[65] G. Kresse and D. Joubert, From ultrasoft pseudopotentials to the projector augmented-wave method, Phys. Rev. B **59**, 1758 (1999).

[66] Pylada computational framework, https://github.com/pylada/pylada-light (2014).

[67] A. Togo and I. Tanaka, Spglib: a software library for crystal symmetry search, arXiv:1808.01590.

[68] W. Setyawan and S. Curtarolo, High-throughput electronic band structure calculations: Challenges and tools, Comput. Mater. Sci. **49**, 299 (2010).

[69] P. Gorai, R. W. McKinney, N. M. Haegel, A. Zakutayev, and V. Stevanovic, A computational survey of semiconductors for power electronics, Energy Environ. Sci. **12**, 3338 (2019).

[70] D. R. Hamann, Optimized norm-conserving Vanderbilt pseudopotentials, Phys. Rev. B **88**, 085117 (2013).

[71] M. van Setten, M. Giantomassi, E. Bousquet, M. Verstraete, D. Hamann, X. Gonze, and G.-M. Rignanese, The PseudoDojo: Training and grading a 85 element optimized norm-conserving pseudopotential table, Comput. Phys. Commun. **226**, 39 (2018).

[72] N. Marzari, A. A. Mostofi, J. R. Yates, I. Souza, and D. Vanderbilt, Maximally localized Wannier functions: Theory and applications, Rev. Mod. Phys. **84**, 1419 (2012).

[73] A. A. Mostofi, J. R. Yates, Y.-S. Lee, I. Souza, D. Vanderbilt, and N. Marzari, wannier90: A tool for obtaining maximally localized Wannier functions, Comput. Phys. Commun. **178**, 685 (2008).

[74] C. Verdi and F. Giustino, Fröhlich Electron-Phonon Vertex from First Principles, Phys. Rev. Lett. **115**, 176401 (2015).

[75] X. Gonze, B. Amadon, P.-M. Anglade, J.-M. Beuken, F. Bottin, P. Boulanger, F. Bruneval, D. Caliste, R. Caracas, M. Cote, and T. Deutsch, ABINIT: First-principles approach to material and nanosystem properties, Comput. Phys. Commun. **180**, 2582 (2009).

[76] A. H. Romero, D. C. Allan, B. Amadon, G. Antonius, T. Applencourt, L. Baguet, J. Bieder, F. Bottin, J. Bouchet, E. Bousquet, and F. Bruneval, ABINIT: Overview and focus on selected capabilities, J. Chem. Phys. **152**, 124102 (2020).

[77] M. Royo and M. Stengel, First-Principles Theory of Spatial Dispersion: Dynamical Quadrupoles and Flexoelectricity, Phys. Rev. X **9**, 021050 (2019).

[78] H. P. Boehm and R. W. Coughlin, Enthalpy difference of hexagonal and rhombohedral graphite, Carbon **2**, 1 (1964).

[79] A. Jain, S. P. Ong, G. Hautier, W. Chen, W. D. Richards, S. Dacek, S. Cholia, D. Gunter, D. Skinner, G. Ceder, and K. A. Persson, Commentary: The Materials Project: A materials genome approach to accelerating materials innovation, APL Mater. **1**, 011002 (2013).

[80] H. A. Wilhelm, B. Croset, and G. Medjahdi, Proportion and dispersion of rhombohedral sequences in the hexagonal structure of graphite powders, Carbon **45**, 2356 (2007).

[81] W. H. Bragg and W. L. Bragg, The structure of the diamond, Proc. R. Soc. London Ser. A **89**, 277 (1913).

[82] F. P. Bundy and J. S. Kasper, Hexagonal diamond - a new form of carbon, J. Chem. Phys. **46**, 3437 (1967).

[83] P. D. Ownby, X. Yang, and J. Liu, Calculated x-ray diffraction data for diamond polytypes, J. Am. Ceram. Soc. **75**, 1876 (1992).

[84] K. E. Spear, A. W. Phelps, and W. B. White, Diamond polytypes and their vibrational spectra, J. Mater. Res. **5**, 2277 (1990).

[85] A. Phelps, W. Howard, and D. Smith, Space groups of the diamond polytypes, J. Mater. Res. **8**, 2835 (1993).

[86] S. F. Matar and V. L. Solozhenko, Crystal chemistry rationale and *ab initio* investigation of utra-hard dense rhombohedral carbon and boron nitride, Diamond Relat. Mater. **120**, 108607 (2021).

[87] B. G. Kim, H. Sim, and J. Park, C4 carbon allotropes with triple-bonds predicted by first-principles calculations, Solid State Commun. **169**, 50 (2013).

[88] K. Umemoto, R. M. Wentzcovitch, S. Saito, and T. Miyake, Body-Centered Tetragonal C_4: A Viable $sp3$ Carbon Allotrope, Phys. Rev. Lett. **104**, 125504 (2010).

[89] A. Belsky, M. Hellenbrandt, V. L. Karen, and P. Luksch, New developments in the Inorganic Crystal Structure Database (ICSD): Accessibility in support of materials research and design, Acta Crystallogr., Sect. B **58**, 364 (2002).

[90] O. Hassel and H. Mark, About the crystal structure of graphite, Z. Angew. Phys. **25**, 317 (1924).

[91] H. W. Kroto, J. R. Heath, S. O'Brien, R. F. Curl, and R. E. Smalley, C60: Buckminsterfullerene, Nature (London) **318**, 162 (1985).

[92] A. Yaghoubi, R. Singh, and P. Melinon, Predicting the primitive form of rhombohedral silicon carbide (9R-SiC): A pathway toward polytypic heterojunctions, Cryst. Growth Des. **18**, 7059 (2018).

[93] L. Ramsdell and J. A. Kohn, Disagreement between crystal symmetry and x-ray diffraction data as shown by a new type of silicon carbide, 10*H*, Acta Crystallogr. **4**, 111 (1951).

[94] T. Yuasa, T. Tomita, and K. Ohta, The crystal structure of SiC 14H, J. Phys. Soc. Jpn. **21**, 2084 (1966).

[95] L. S. Ramsdell and R. S. Mitchell, A new hexagonal polymorph of silicon carbide, 19H, Am. Mineral. **38**, 56 (1953).

[96] W. Hujo, B. S. Jabes, V. K. Rana, C. Chakravarty, and V. Molinero, The rise and fall of anomalies in tetrahedral liquids, J. Stat. Phys. **145**, 293 (2011).

[97] P. Petroff, A. C. Gossard, and W. Wiegmann, Structure of AlAs-GaAs interfaces grown on (100) vicinal surfaces by molecular beam epitaxy, Appl. Phys. Lett. **45**, 620 (1984).

[98] H. J. Ko, Y. F. Chen, T. Yao, K. Miyajima, A. Yamamoto, and T. Goto, Biexciton emission from high-quality ZnO films

grown on epitaxial GaN by plasma-assisted molecular-beam epitaxy, Appl. Phys. Lett. **77**, 537 (2000).

[99] J. A. Perri, S. LaPlaca, and B. Post, New group III-group-V compounds: BP and BAs., Acta Crystallogr. **11**, 310 (1958).

[100] H. Karzel, W. Potzel, M. Kófferlein, W. Schiessl, M. Steiner, U. Hiller, G. M. Kalvius, D. W. Mitchell, T. P. Das, P. Blaha *et al.*, Lattice dynamics and hyperfine interactions in ZnO and ZnSe at high external pressures, Phys. Rev. B **53**, 11425 (1996).

[101] A. M. Khar'kova and T. Ya. Velikanova, Structure of the alloys of the system rhenium-carbon in the region rich with rhenium, Sov. Powder Metall. Metal Ceram. **26**, 994 (1987).

[102] C. P. Kempter and M. Nadler, Preparation and crystal structures of RuC and OsC, J. Chem. Phys. **33**, 1580 (1960).

[103] F. Birch, Finite elastic strain of cubic crystals, Phys. Rev. **71**, 809 (1947).

[104] F. D. Murnaghan, Finite deformations of an elastic solid, Am. J. Math. **59**, 235 (1937).

[105] J. C. Phillips, Ionicity of the chemical bond in crystals, Rev. Mod. Phys. **42**, 317 (1970).

[106] R. Zarnetta, R. Takahashi, M. L. Young, A. Savan, Y. Furuya, S. Thienhaus, B. Maaß, M. Rahim, J. Frenzel, H. Brunken *et al.*, Identification of quaternary shape memory alloys with near-zero thermal hysteresis and unprecedented functional stability, Adv. Funct. Mater. **20**, 1917 (2010).

[107] Y. Song, X. Chen, V. Dabade, T. W. Shield, and R. D. James, Enhanced reversibility and unusual microstructure of a phase-transforming material, Nature (London) **502**, 85 (2013).

[108] D. Sheppard, P. Xiao, W. Chemelewski, D. D. Johnson, and G. Henkelman, A generalized solid-state nudged elastic band method, J. Chem. Phys. **136**, 074103 (2012).

[109] Y. Wu, J. Kang, and F. Liu, Pressure induced wurtizte-to-zinc blende phase transition in ZnO at finite temperature, J. Mater. Res. **23**, 3347 (2008).

[110] Ioffe semiconductor database, http://www.ioffe.ru/SVA/NSM/Semicond/SiC/hall.html.

[111] A. Seidl, A. Gorling, P. Vogl, J. A. Majewski, and M. Levy, Generalized Kohn-Sham schemes and the band-gap problem, Phys. Rev. B **53**, 3764 (1996).